Local disorder and structure relation induced by magnetic exchange interactions in $A_2(Mo_{1-y}Mn_y)_2O_7$ pyrochlores

C. Castellano[a,*], M. Scavini[a], G. Berti[b], F. Rubio-Marcos[c,d], G. Lamura[e], S. Sanna[f], E. Salas-Colera[g,h,i], Á. Muñoz-Noval[l], M. R. Cimberle[e], F. Demartin[a]

[a] *Dipartimento di Chimica, Università degli Studi di Milano, via Golgi 19, 20133 Milano, Italy*
[b] *Institut National de la Recherche Scientifique, Centre Énergie Matériaux Télécommunication, 1650 Boulevard Lionel-Boulet, Varennes (Québec) J3X 1S2 Canada*
[c] *Electroceramic Department, Instituto de Cerámica y Vidrio, CSIC, Kelsen 5, 28049 Madrid, Spain*
[d] *Escuela Politécnica Superior. Universidad Antonio de Nebrija, Pirineos 55, 28040, Madrid, Spain*
[e] *CNR-SPIN, c/o Dipartimento di Fisica, University of Genoa, Via Dodecaneso 33, 16146 Genova, Italy*
[f] *Department of Physics and Astronomy, University of Bologna, 40127 Bologna, Italy*
[g] *Instituto de Ciencia de Materiales de Madrid, ICMM, CSIC, Sor Juana Inés de la Cruz 3, 28049, Cantoblanco, Madrid, Spain*
[h] *Spanish CRG BM25 SpLine, ESRF 71 Avenue des Martyrs CS 40220 FR - 38043 Grenoble, France*
[i] *Departamento de Física, Universidad Carlos III de Madrid (UC3M), Av. de la Universidad 30, 28911, Leganés, Madrid, Spain*
[l] *Departamento de Física de Materiales, Facultad de CC. Físicas, Universidad Complutense de Madrid, Pza. de Ciencias, 1 - 28040 Madrid, Spain*

*Corresponding author. E-mail address: carlo.castellano@unimi.it

ABSTRACT

We present an extended X-ray absorption fine structure study at the Mo *K*-edge of $A_2(Mo_{1-y}Mn_y)_2O_7$ (*A* = Gd, Ho; y = 0.05 and 0.10) pyrochlores, as a function of temperature and composition, coupled to diffractometric and magnetic characterizations. Extending the study reported in our previous paper on the pristine $A_2Mo_2O_7$ compounds to these Mo/Mn partially substituted samples, where we hypothesize a competition between double-exchange and superexchange couplings, we aim to check which structure parameters are related to the nature of the nearest-neighbor magnetic interactions, looking for the presence and evolution of order and structure anomalies. Two Ho samples $Ho_2(Mo_{1-y}Mn_y)_2O_7$ (y = 0.05 and 0.10) keep the spin-glass nature of the parent compositions with a strong distortion of the $MoO(1)_6$ octahedron and of the Mo-Ho and Mo-Mo second shell. On the other hand, two $Gd_2(Mo_{1-y}Mn_y)_2O_7$ samples, ferromagnetic at low temperature in the undoped case, show the appearance on a local scale of a spin-glass transition mirrored by a quite high structure disorder and by a distortion coherent with a lattice frustration after Mn-doping.

Therefore, the Gd and Ho Mn-doped samples display a similar frustrated behaviour, differently from the corresponding undoped ones.

Keywords: A. Oxide materials; C. Order-disorder effects; C. Exchange and superexchange; D. EXAFS; D. X-ray diffraction

1. Introduction

Pyrochlores are complex and multifunctional oxides having general formula $A_2^{3+}B_2^{4+}O(1)_6(O2)$, where *A* is a trivalent rare-earth ion including lanthanides, Y, or Sc and *B* is a tetravalent transition metal ion [1,2]. Due to their several possible compositions, pyrochlores offer a wide range of interesting and challenging physical properties and potential technological applications. These compounds can be employed as insulators, ion and electron conductors, superconductors, catalysts, ion exchangers, reading-writing magnetic memories, phosphors and solid-oxide fuel cells cathodes [1-5]. Recently, their highly versatile nature has been further investigated by numerous studies performed on grain size correlated electrical properties [6], phase stability of nuclear waste forms [7,8], oxide dispersion strengthened steel-based alloys (ODS) [9], promising thermal barrier coatings modulation [10], upconversion luminescence and optoelectronic/electrophysical properties [11,12].

The *A* and *B* cationic sites form a network of corner-sharing tetrahedra characteristic, in presence of competing magnetic interactions, of short-range ordered geometrically frustrated phases at low temperatures, such as spin glasses, spin ices and spin liquids [13]. Indeed, the everlasting order/disorder competition observed in these strongly correlated electron oxides, permanently coupled with different magnetic exchange couplings and interactions, plays a pivotal role in tuning their physico-chemical properties [3-5]. This is the starting point of the structural and magnetic study at the basis of this paper on new Mo/Mn partial substitutions in the parent $A_2Mo_2O_7$ compositions.

In our previous paper [14], we devoted special attention to those pyrochlores where glassy transitions instead of a long-range magnetic order occur upon varying the chemical composition and temperature, mainly due to spin-spin and neighbor exchange interactions. More in detail, we studied the ferromagnetic (FM) $Gd_2Mo_2O_7$ and three spin-glass (SG) $A_2Mo_2O_7$ (with *A* = Dy, Ho, Er) compounds [14,15]. Since in complex oxides it is well established that the *B*-O-*B* bond angle affects the magnitude and sign of the magnetic exchange interaction between the neighboring *B* ion spins, the mean rare earth ionic radius r_A influences the magnetic ground state, i.e. the FM or SG phase [16,17]. In $A_2Mo_2O_7$ pyrochlores having two 4*d* electrons accommodated in the t_{2g} orbitals of Mo^{4+} ions, the FM interaction between the Mo spins has been interpreted in terms of the double-exchange mechanism, thus observing the transition from the SG insulating state to the FM metallic one upon increasing the average ionic radius r_A and the related Mo-O-Mo bond angle [15,18]. A

metal-insulating transition takes place around the $Gd_2Mo_2O_7$ composition, which is an insulator in the ground state being on the phase boundary between the SG and the FM regimes [15,19]. The FM transition is also accompanied by magnetic irreversibility [20]. In this context, Shinaoka *et al.* pointed out, by relativistic DFT plus on-site repulsion (U) method, that in these systems the effective spin interactions are more complex than the simple Heisenberg form and are strongly anisotropic in spin space, giving rise to intense competition between antiferromagnetic and ferromagnetic states [21].

On the other hand, Shimakawa *et al.* systematically investigated the Mn-O-Mn bond angle θ behavior in the Mn-pyrochlores $A_2Mn_2O_7$ (*A* = In, Lu, Tl, and Y) proving that, differently from the Mo case, the Kanamori-Goodenough's rule is followed and the superexchange interaction between Mn^{4+} ions via oxygen atoms strongly increases as a function of the Mn-O-Mn bond angle [16,17]. An antiferromagnetic (AFM) superexchange interaction occurs for greater bond angles and on increasing r_A, while a FM interaction is observed towards a 90° arrangement of the $(3d)^3$ spins. Summarizing, larger r_A values determine in all pyrochlore systems a different steric hindrance and therefore an increase of the *B*-O-*B* bond angle as well as of the *B*-O bond length. At the same time, they promote magnetic orderings, which are based on a FM ground state in the *B* = Mo case and AFM in the *B* = Mn one [15,16].

It was also pointed out that both SG and FM components seem to coexist near the phase boundary of the corresponding phases [22,23], and a re-entrant SG transition was observed at lower temperatures and below T_C, for *A* = Nd and Sm [23-25].

In this general scenario, we stated that the magnetic state transition from FM to SG should be driven by the competing double-exchange and superexchange interactions in the frustrated structure [14,26,27]. To validate this interpretation, it would be interesting to vary the relative strength of these two different spin-spin couplings. Doping materials showing either FM or SG interactions, such as $Gd_2Mo_2O_7$ and $Ho_2Mo_2O_7$ respectively, with a suitable dopant like Mn at the *B* site, can help to achieve this effect. We can reasonably assume that the partial Mo^{4+}/Mn^{4+} ion substitution could determine and emphasize a competition and modulation of the two mentioned magnetic exchange interactions. This outcome is achieved due to the influence of the different ionic radii of Mo^{4+} and Mn^{4+} ions on the conduction bandwidth along the Mo-O-Mo or Mn-O-Mn bond lengths, respectively.

Consequently, in order to determine which crystal structure parameters are affected by the Mn doping and related competition of the nearest-neighbor magnetic interactions, we report here a systematic and original investigation of the local structure of $A_2(Mo_{1-y}Mn_y)_2O_7$ pyrochlores (with A = Gd and Ho; y = 0.05 and 0.10) by temperature-dependent extended X-ray absorption fine structure (EXAFS) measurements.

2. Experimental methods and data analysis

Synthesis. Appropriate amounts of the precursors A_2O_3 (Metal Rare Earth Limited, 99.5%), MoO_2 and MnO_2 (Sigma–Aldrich, 99.9%), were weighed and mixed to obtain powder samples of $A_2(Mo_{1-y}Mn_y)_2O_7$ pyrochlore compounds by conventional solid-state reaction using different rare-earths (A), namely $A = Ho^{3+}$ and Gd^{3+}. Furthermore, six compositions were synthesized based on the Mo/Mn concentration, which can be described by the general formula $A_2(Mo_{1-y}Mn_y)_2O_7$ where y takes the following values: 0.03, 0.05 and 0.10. The mixtures were mechanically homogenized by ball milling for 3 hours in ethanol medium in a turbula-type mixer with ZrO_2 balls with a diameter of 0.5 mm. Subsequently, the powder mixtures were heated to 950 ºC for 4 hours at a rate of 100 ºC/min under Ar atmosphere. Finally, the resulting powders were milled again for 3 hours, and the last heat treatment was performed in Ar atmosphere at 1350 ºC for 8 hours for all compositions.

Since both Mo and Mn may have different oxidation states, oxidizing (air or oxygen) or reducing atmospheres (nitrogen/hydrogen) can induce oxidation and reduction processes thus modifying dramatically the chemical composition and crystalline structure of the systems. For this reason, the selection of a neutral/inert atmosphere such as the Ar one was found to be preferable (as already reported in Refs. 15 and 22).

X-ray diffraction. An essential determination of the phase crystalline (that is, cubic symmetry) was accomplished using in-house X-ray diffraction (XRD, X'Pert PRO Theta/2theta of Panalytical, PANalytical, The Netherlands), see the Supplementary Material (SM) for details. The X-ray diffraction data were collected in the range $5° \leq 2\theta \leq 90°$ with a step length of 0.0334° and a step counting time of 100 s using Cu K_α radiation (λ = 0.154056 nm) with working voltage and current of 40 kV and 100 mA, respectively, at room temperature. X-ray diffraction refinement peaks were performed using the Checkcell program [28], supposing a pseudo-Voigt peak function for the profile fitting. Unit cell parameters were refined by a global

simulation of the full diagram (pattern matching, PEAKOC program) assuming a face-centered cubic symmetry (*fcc*) and space group $Fd\bar{3}m$ [29]. About the structural evolution, more detailed information can be found in Supplementary Material S1.

Magnetic characterization. The magnetic behavior of all the samples under study, namely y = 0.03, 0.05 and 0.10, was checked by dc magnetometry measured by a commercial dc-squid (MPMS2 by Quantum Device). The experimental results are detailed in section 3.2 and in the Appendix.

High-resolution powder diffraction. High-resolution X-ray powder diffraction patterns in the 10-300 K range have been collected on the pure compounds and on the y = 0.10 solid solutions during experiment HC-3343 at the Spanish beamline (BM25A) at the ESRF using a wavelength λ=0.477897(3) Å [30]. Samples were put in Ø = 0.5 mm glass capillaries and inserted in a liquid He cryostat. Measurements have been carried out in the $2° \leq 2\theta \leq 50°$ range, corresponding to a maximum modulus of the scattering vector $Q = 4\pi\sin\theta/\lambda$ as large as 11.1 $Å^{-1}$. Denser *T* grids were used for $T \leq 100$ K to test possible structural phase transition in correspondence to the magnetic ones.

The Rietveld refinements have been carried out using GSAS suite of programs and its graphical interface Expgui [31]. In the final refinements, cell constants, zero error, the phase scale factor, selected peak shape parameters (pseudo-Voigt functions), one average atomic mean square displacement parameter and the x_{O1} coordinate have been allowed to vary. In Fig. S1 the Rietveld refinement of sample $Gd_2(Mo_{0.90}Mn_{0.10})_2O_7$ collected at 30 K is shown as an example.

EXAFS measurements. The EXAFS measurements were carried out on the $A_2(Mo_{1-y}Mn_y)_2O_7$ samples with y = 0.05 and 0.10 at the Mo *K*-edge (20000 eV) in transmission geometry at the European Synchrotron Radiation Facility (ESRF) on beamline BM25A, using a double Si(111) crystal monochromator of the pseudo channel-cut type refrigerated at 200 K by a homemade ethanol cooling system. The energy resolution given by the monochromator was 1.2 eV. The polycrystalline $A_2(Mo_{1-y}Mn_y)_2O_7$ pyrochlores were dispersed in a cellulose matrix and pressed into pellets, for optimizing the jump at the absorption edge. To accurately follow the behavior of the local order and structure parameters as a function of temperature, we measured accurate spectra at about 30 different temperatures in the range 5-300 K for both the samples. An Oxford CV-F optistat liquid helium (LHe) cryostat with a LHe Dewar supply was used (at least three scans were

collected at each temperature for averaging and checking the reproducibility). Examples of the resulting high-quality *k*-space data at several temperatures and up to 15 $Å^{-1}$ are shown in Fig. 1.

The EXAFS data were reduced using the Demeter package standard procedures [32]; fits of the k^2 weighted EXAFS data were carried out in *r* space using theoretical functions from the FEFF9 code [33].

To include the first and further neighbors in fitting the data (full *R*-fit range: 0.75 – 3.82 Å), we used the first shell Mo-O(1) peak with *R* = 2.01 Å bond length and coordination number $N_{Mo\text{-}O(1)}$ = 6 (at 300 K), the Mo-Mo and Mo-*A* second shell peaks (N = 6 each) and one multiscattering peak. The latter was the triple forward scattering through the absorber Mo–O(1)–Mo–O(1)–Mo (N = 6), the most intense multiple scattering contribution due to the focusing effect. Alternatively, two first subshells Mo-O(1) (with coordination numbers $N_{shorter}$ = 2, N_{longer} = 4 and lengths $R_{shorter}$ = 1.90 Å, R_{longer} = 2.00 Å, respectively, still at 300 K) were used, consistently with the predisposition of pyrochlores towards *B*-site octahedron distortion [1,34-36].

An overview of all the paths used in our fits is shown in Fig. 2, where it is possible to appreciate their different trend as a function of the momentum transfer *q*. The initial fitting parameters were the mean-square disorder in the neighbor distances σ^2 (or "Debye-Waller parameter"), the interatomic distances *R*, the E_0 shift in the edge energy with respect to the theoretical value and the amplitude reduction factor S_0^2 from multielectron effects. This last factor is generally between 0.8 and 1.0. At low *T*, the lattice is well ordered, and S_0^2 was determined from the average of several fits to scans at 8 K and fixed at 0.96. The E_0 shift was also constrained to a single value for all paths. In order to have not too many independent parameters and to limit the correlations among them, the σ^2 of the two subshells were linked to be equal to one another and the interatomic distance of the multiscattering peak was constrained to the structure [15,37,38]. The coordination numbers were fixed to the previously reported values for the first shell and to the crystallographic values for all the other shells and paths employed in the fit, thus reducing the uncertainty on the σ^2 parameters. This uncertainty on the local order was calculated as the statistical variance of the σ^2 parameter values obtained from the fits on the different scans collected at the same temperature, for each sample. The parameters to be varied were the remaining unconstrained σ^2, *R* and a single E_0 shift.

3. Results and discussion

3.1 High-resolution powder diffraction

High-resolution powder diffraction measurements have been performed for y = 0.00 and 0.10. All the measurements point out the presence of the undistorted pyrochlore $A_2B_2O_7$ cubic phase, space group N° 225 $Fd\bar{3}m$ [1]. Pyrochlore structure derives from the fluorite one (formula MO_2, space group N° 225 $Fm\bar{3}m$) where tetravalent *M* ions form a cubic close packed structure and O ions occupy all the tetrahedral sites. Oxygen vacancies formation and ordering, coupled to cation ordering, cause the symmetry decrease.

Selecting the origin choice nr. 2 of the International Tables of Crystallography, within pyrochlore structure, *A*(= Gd/Ho) cations occupy the (½, ½, ½) site at 16*d* (site multiplicity plus Wyckoff letter), *B*(=Mo/Mn) cations the (0, 0, 0) site, at 16*c*. Oxygen ions are distributed in two crystallographic non-equivalent sites: O1(x_{O1}, ⅛, ⅛) at 48*f* and O2 (⅜, ⅜, ⅜) at 8*b*. Therefore, x_{O1} is the only structural degree of freedom.

A cations are surrounded by 2 closer O2 and 6 farther O1 ions ($d_{A\text{-}O2}$≈2.2 Å $d_{A\text{-}O1}$≈2.5 Å, in the investigated compounds) forming a cubic distorted cage. *B* cations are surrounded by 6 O1 ions at the same interatomic distance $d_{B\text{-}O1}$ ≈ 2.0 Å, forming an octahedral distorted cage. It should be noted that undistorted cubic and octahedral cages appear for x_{O1}=3/8 and 5/16, respectively [1].

As mentioned above, the *A* and *B* cations are in special positions and form a network of corner-sharing tetrahedra. All *A*-*B*, *A*-*A* and *B*-*B* distances (multiplicity equal to 6, each) are equal with $d_{A\text{-}A/A\text{-}B/B\text{-}B}$≈3.6-3.7 Å in the present compounds.

Fig. S1 of the Supplementary Material reports, as an example, the experimental patterns collected at 30 K on $Gd_2(Mo_{0.90}Mn_{0.10})_2O_7$ sample (black crosses) and the Rietveld refinement (red curve) and Table S1 summarizes the results of the Rietveld refinements of patterns collected at 10 K on all the samples.

The diffraction patterns of the pure samples (*A* = Gd/Ho, y = 0.00) reveal that they are monophasic, confirming the standard X-ray diffraction results [14,15], and no phase transitions appear in the $10 \leq T \leq 300$ K range. The trend of the cell constant *a*, x_{O1} and the average atomic means square parameters versus *T* are shown in Fig. 3 for *A* = Gd and Ho as black circles and diamonds, respectively.

Moreover, in Fig. 3 the Rietveld refined structural parameters of the pyrochlore phase for all the samples are reported. As displayed in Fig. 3a, the cell constant *a* increases going from the *A* = Ho to the *A* = Gd

compound, as expected for the larger ionic radius of Gd^{3+}(VIII) compared with Ho^{3+}(VIII): 1.053 and 1.015 Å, respectively [39]. Mn doping of both compounds causes cell shrinking. At 10 K, $\frac{a_{pure}-a_{doped}}{a_{pure}} \cdot 100\%$ is 0.38% for *A* = Gd and 0.63% for *A* = Ho suggesting that Mn enters in the pyrochlore structure, despite the presence of the spurious phase (see also Fig. S2 of the SM). Due to the reduced cell volume, manganese should enter in the structure either as Mn^{4+} or as low spin (LS) Mn^{3+}. In fact, the ionic radii (*ir*) of Mn^{4+}(VI) and $Mn^{3+}(VI)_{LS}$ (0.53 and 0.58 Å, respectively) are smaller than that of Mo^{4+}(VI)= 0.65 Å; we can exclude the presence of High Spin Mn^{3+}(VI) since its *ir* is 0.645 Å [39].

The x_{O1} coordinate, shown in Fig. 3b, does not display any clear dependence on *T*. Despite some spread of its values, on average, in the Gd containing samples the AO_8 cubic cage should be less distorted than in the *A* = Ho cases. In Table 1 the shortest cation-oxygen and cation-cation interatomic distances are reported for all the samples at 10 K, calculated starting from *a* and x_{O1} values. These "average" distances, related to the average structure, will be compared to the EXAFS "local" results. We should warn the reader that the small errors on the quantities in Table 1 are related to the small standard deviations on the cell constants supplied by the Rietveld refinements (see Table S1 of the SM) coupled to the special positions (no positional degrees of freedom) of the *A* and Mo sites.

Table 1. Shortest cation-oxygen and cation-cation interatomic distances at 10 K (in Å). *A* = Gd, Ho; *B* = Mo/Mn.

	$Gd_2(Mo_{1-y}Mn_y)_2O_7$		$Ho_2(Mo_{1-y}Mn_y)_2O_7$	
	y=0.00	y=0.10	y=0.00	y=0.10
A-O1 × 6/Å	2.49460(1)	2.490(8)	2.455(7)	2.464(8)
A-O2 × 2/Å	2.24236(1)	2.23385(2)	2.22327(1)	2.20925(2)
B-O1 × 6/Å	2.03788(1)	2.027(5)	2.033(5)	2.004(5)
A-*A* × 6/Å	3.66176(1)	3.64787(3)	3.63058(2)	3.60768(3)
A-*B* × 6/Å	3.66176(1)	3.64787(3)	3.63058(2)	3.60768(3)
B-*B* × 6/Å	3.66176(1)	3.64787(3)	3.63058(2)	3.60768(3)

Finally, the average atomic mean square displacement parameters U_{ave} have quite robust trends as a function of composition, at least at low T values (see Fig. 3c). In particular, U_{ave} takes larger values i) for the doped samples in respect to the pure compounds and ii) for A = Ho in respect to A = Gd.

The thermal and compositional evolution of atomic displacement parameters in solid solutions, compared to pure compounds, is an effective tool to probe the disorder induced by doping [40-42]. We suppose that the different ionic radius of Mn^{4+}(VI) in respect of Mo^{4+}(VI) causes interatomic distance fluctuations around the B site bringing to an increase of the atomic displacement parameters. Unfortunately, attempts to use different U values for each crystallographic site, which could supply a more accurate picture of disorder, brought to correlations among parameters.

3.2 Magnetic measurements

Fig. 4 shows the magnetic transition temperatures as a function of the Mn content for A = Gd and Ho in the left and right panel, respectively, at low field (full symbol) and high field (open symbol). The FM transition temperature, T_p, is determined as the peak of the first derivative in the ZFC magnetization curves. We define $T_{ZFC\text{-}FC}$ as the temperature at which the ZFC and FC curves split, as detailed in the Appendix.

The $T_{ZFC\text{-}FC}$ for A = Ho is typically taken as the freezing temperature T_f. It displays negligible changes as a function of the Mn doping and a sizeable reduction when the magnetic field is increased, as expected for a pure spin-glass phase. On the other hand, the data for A = Gd show a significant effect of Mn doping. Both T_p and $T_{ZFC\text{-}FC}$ reduce and eventually approaches the value of the freezing temperature of the Ho compound for high Mn content. In addition, for low Mn content the magnetic transition temperatures are almost field independent (open and solid symbols coincides within the errorbar for y = 0, 0.03 samples with H = 10 Oe and 10 kOe), whereas for y = 0.05 and 0.10 a strong field dependence similar to the case of A = Ho is observed. This behavior clearly indicates that the Mn doping greatly weakens the full FM ground state of $Gd_2(Mo_{1-y}Mn_y)_2O_7$, characteristic of undoped $A_2Mo_2O_7$ with A lanthanides having the ion size equal or greater than that of Gd, driving the system towards the spin-glass character typically observed when A has a smaller radius than Gd [1,15,21,43]. A similar effect is observed by applying external pressure [44], placing the $Gd_2(Mo_{1-y}Mn_y)_2O_7$ at the border of the FM and spin-glass boundary. The Mn-induced gradual suppression of the FM character for A = Gd is also evidenced by the smooth decrease of the Curie Wiess

temperature θ_{CW} as a function of Mn content, displayed in the Appendix in Fig. A.4b. On one hand, the fact that the θ_{CW} remains positive and the small hysteresis present for all the Mn concentrations (see Fig. A.6 in the Appendix) indicate that the FM correlations, albeit strongly weakened, are still persistent for all the Gd samples. On the other hand, the strong reduction of the magnetic transition, which approaches the value of the spin freezing temperature of the Ho series, and the high magnetic field dependence of T_{ZFC-FC} observed for y = 0.05 and 0.10 indicate that the Mn doping promotes and enhances the spin-glass character at expenses of the FM one.

See the Appendix for further experimental details.

3.3 EXAFS

In Fig. 5 the local order parameter (or shell interatomic distance variance) σ^2 for the Mo-O(1) first coordination shell obtained from the EXAFS fit performed with one subshell, is reported as a function of temperature for the two pure compounds (see Fig. 5a) and for the four $A_2(Mo_{1-y}Mn_y)_2O_7$ solid solutions (see Fig. 5b).

The σ^2 parameter follows a temperature dependent correlated Debye-like model σ_D^2 at high temperatures, characterized by a correlated Debye temperature θ_D (that is around 800 K in these oxides) and a temperature independent static contribution σ_S^2 due to the presence of a possibly distorted environment [35,46]. The high temperature local order parameter was fitted considering $\sigma^2(T) = \sigma_D^2 + \sigma_S^2$, as shown in Fig. 4a and already reported in previous papers [14,34,36,47], where the temperature dependent dynamic contribution σ_D^2 is expressed as an infinite series whose first and most important terms are [36,47]:

$$\sigma_D^2 = \frac{3\hbar^2}{Mk_B\theta_D}\left[\frac{1}{4} + \left(\frac{T}{\theta_D}\right)^2 \int_0^{\frac{\theta_D}{T}} dx \frac{x}{e^x - 1}\right] \quad (1)$$

where M is the mass of the diffuser atom and k_B is the Boltzmann constant. This model, based on σ_D^2 plus a static offset σ_S^2, usually results to be a good approximation for all the phonon modes [48,49]. The fitting parameters were θ_D, which is a measure of the Mo-O(1) bond strength and the static offset σ_S^2. The obtained values are reported in Table 2.

Table 2. Correlated Debye temperature θ_D and static offset σ_S^2 for the first shell Mo-O(1).

Compound	σ_S^2 (Å^2)	θ_D (K)
$Gd_2(Mo_{0.95}Mn_{0.05})_2O_7$	0.0131(3)	794(43)
$Gd_2(Mo_{0.90}Mn_{0.10})_2O_7$	0.0065(3)	796(37)
$Ho_2(Mo_{0.95}Mn_{0.05})_2O_7$	0.0061(3)	790(47)
$Ho_2(Mo_{0.90}Mn_{0.10})_2O_7$	0.0066(3)	794(47)

All the compositions display a correlated Debye-like trend at all the temperatures within the investigated range (Fig. 5). The Debye temperatures are in accordance with other pyrochlore compounds [34,35,50,51].

In manganese free $Gd_2Mo_2O_7$ and $Ho_2Mo_2O_7$ phases, the σ_S^2 static contribution was σ_S^2= 0.0032(3) and 0.0053(3) Å^2, respectively [14]. The larger σ_S^2 value of the latter Ho-based compound was attributed to the structural frustration induced by its long-range SG magnetic behavior, absent in this form in FM $Gd_2Mo_2O_7$. Moreover, our magnetic measurements revealed a SG behavior also in Mn doped samples (see the Appendix). The increase of σ_S^2 values in these solid solutions should be attributed to the structural disorder introduced by Mn doping, in agreement with diffraction results (see Fig. 3).

Therefore, the step increase of σ_S^2 values in $Gd_2(Mo_{1-y}Mn_y)_2O_7$ solid solutions with respect to $Gd_2Mo_2O_7$ compound should be due to the sum of two different contributions: i) Mn doping at the Mo site (as in the *A* = Ho series) and ii) the progressive transition from FM to SG on increasing the doping. This last outcome is also testified by magnetic measurements shown in the previous section and in the Appendix. At the same time, the anomalous local–structure disorder we observed in $Gd_2Mo_2O_7$ below 225 K [6], now disappears. Anyway, the $Gd_2(Mo_{0.95}Mn_{0.05})_2O_7$ less doped sample presents a higher σ_S^2 = 0.0131 Å^2, consistent with its proximity to the FM/SG compositional transition [14].

Our magnetic and structural results suggest that there is a frustration effect due to the Mn doping on the Mo site mainly because Mo gives rise to a double-exchange mechanism whereas Mn to superexchange. Therefore, the most doped Gd and Ho samples finally assume a similar local structure behaviour, differently from the corresponding undoped compounds.

In our previous paper, we already stated how the influence of frustration on the local structure of the undoped and peculiar $Gd_2Mo_2O_7$ composition is somewhat surprising since the prevalent coupling between metallic ions on the *B*-sites is FM and we hypothesized that further AFM neighbouring interactions would play an important role [14,26,52]. Moreover, Mössbauer spectroscopy, neutron diffraction and muon spin relaxation (μSR) measurements already showed in $Gd_2Mo_2O_7$ an abnormal FM state with spin fluctuations similar to those present in spin-liquid-like systems [26,52].

In the present paper, observing the appearance and strengthening of a low temperature disordered SG phase component and magnetic exchange competition after Mo/Mn partial substitution, we prove that this supposition was rightly founded.

In order to gain a deeper insight of the structural disorder in the explored solid solutions, we subsequently hypothesized the presence of at least a bimodal distribution of the Mo-O(1) interatomic distances in the first shell $MoO(1)_6$ octahedra. This structure distortion is consistent with the two subshell fit model described in our previous paper on the undoped compounds [6] and with the Mo-(Mo/*A*) bond lengths behavior. The results of these fits are displayed in Figs. 6 and 7, respectively.

As displayed in Fig. 6, our EXAFS fits reveal two shorter apical and four longer basal first shell Mo-O(1) interatomic distances. This behavior indicates that an octahedral distortion and symmetry breaking is present for all the studied compositions even if reduced compared to the undoped ones. In accordance, Higashiya et al. (2007) showed in $A_2Mo_2O_7$ with *A* = Nd, Sm, Gd, Tb and Y, that the $MoO(1)_6$ octahedron should be further trigonally distorted pushing together one pair of opposite faces [53,54].

In the *A* = Ho series, the difference between the Mo-O distances of the two subshells ΔR (≈ 0.11 Å) is almost unaffected by doping; conversely, in the *A* = Gd series the starting value of ΔR ≈ 0.18 Å in the pure compound, raises to ≈ 0.21 Å for y= 0.05 and turns to smaller values (≈ 0.11 Å), for y = 0.10.

Therefore, as for the σ_S^2 values, the $Gd_2(Mo_{0.95}Mn_{0.05})_2O_7$ less doped sample presents a different behaviour with respect to all the other three studied Mn-doped compounds. This outcome could be due to an expected smaller effect of the Mn doping for the lower y = 0.05 composition which is still characterized by some criticalities of $Gd_2Mo_2O_7$, located on the border between the SG and the FM regimes [14,25,26,52].

We point out that the difference between the two Mo-O(1) subshells is at least of about 0.110 Å, i.e. well above the widely recognized ΔR limit determined by the EXAFS resolving power between two scattering

shells involving the same chemical species at different distances, $\Delta R \geq \pi/2k_{max}$, where k_{max} is the maximum k vector used. Since for our data k_{max} = 15 Å^{-1}, we are able to accurately resolve splittings down to 0.105 Å [55,56].

The Mo-*A* and Mo-Mo interatomic distances are reported in Fig. 7. According to the crystallographic structures, they should be all identical to each other (see Table 1). Conversely, EXAFS analysis shows that in all the solid solutions each Mo ion is surrounded by six shorter Mo-*A* and six longer Mo-Mo ions. This splitting of metal-metal distances raises upon doping and with smaller *A* ion. In fact, ΔR is ≈ 0.08, 0.10, 0.15 and 0.20 Å for $Gd_2(Mo_{0.95}Mn_{0.05})_2O_7$, $Gd_2(Mo_{0.9}Mn_{0.10})_2O_7$, $Ho_2(Mo_{0.95}Mn_{0.05})_2O_7$ and $Ho_2(Mo_{0.9}Mn_{0.10})_2O_7$, respectively.

Moreover, the local order parameters $\sigma^2(T)$ related to these second coordination shells have a monotonic behaviour and do not show any anomaly in the one subshell fit, as already observed in the undoped compositions [14].

In this context, the diffraction and EXAFS structural findings support each other. The crystallographic structures of pyrochlore phases stay cubic and undistorted in the whole *T* and *y* ranges investigated, implying single Mo-O and Mo-Mo/Gd first and second coordination shells, respectively; conversely, EXAFS reveals bimodal distributions of Mo-O distances in all the samples, flanked by bimodal Mo-Mo/Gd ones in the solid solutions. These results are reconciled supposing a short coherence length of the symmetry breaks revealed by EXAFS for both *A* = Gd and Ho systems. When the local fluctuations of the Mo-Mo/Gd interatomic distances in the solid solutions are averaged in the crystallographic structure, they are no longer measurable by XRD even if enlarged atomic mean square displacement parameters are revealed by the Rietveld analysis of the diffraction patterns.

4. Conclusions

We have performed a temperature dependent EXAFS study at the Mo *K*-edge on four manganese doped Mo-based pyrochlores $A_2(Mo_{1-y}Mn_y)_2O_7$ (*A* = Gd and Ho) coupled to high-resolution powder diffraction and magnetic measurements providing relevant information on the local and average structure and on the magnetic properties of the investigated compounds.

The magnetic and structural measurements show that there is a frustration effect induced by both the Mo/Mn doping and the competition between the double-exchange mechanism due to Mo ions and the superexchange one due to Mn ions. Therefore, the frustrated SG phase component is strengthened at the expenses of the FM one and all the Mn doped samples finally assume a similar behaviour, differently from the corresponding undoped compounds.

EXAFS analysis reveals that the $Gd_2(Mo_{0.95}Mn_{0.05})_2O_7$ less doped sample presents a higher σ_S^2 static disorder contribution and the two apical interatomic Mo-O(1) distances even shorter and more similar to those obtained in the undoped $Gd_2Mo_2O_7$ which is characterized by some criticalities due to its location on the border between the SG and the FM regimes.

Moreover, a local distortion is observed for all the studied compositions, pointing out two shorter and four longer first Mo-O(1) subshells, as in the undoped samples [14], as well as six shorter Mo-*A* and 6 longer Mo-Mo interatomic distances, in the framework of the competition between order and disorder, typical of pyrochlores [34,57]. These findings are reconciled with the undistorted pyrochlore structure revealed by X-ray powder diffraction in the whole *T* and composition ranges supposing a short coherence length of the symmetry breaks revealed by EXAFS.

We already emphasized how in $Gd_2Mo_2O_7$ this order/disorder competition gives rise to unique features in the local structure [14,34]; now, after Mn-doping, the SG disordered component finally prevails. Therefore, the frustrated SG phase is always in the pyrochlores background and becomes dominant in these doped chemical compositions.

Acknowledgments

We gratefully acknowledge the Spanish CRG at the ESRF for providing beamtime under experiment HC-3343. MS thanks Prof. Monica Dapiaggi for useful discussions. GL thanks Prof. Fabio M. Canepa for illuminating discussions. F.R.-M. gratefully acknowledge the support of the AEI (Spanish Government) Project (Nos. MAT2017-86450-C4-1-R). F.R.-M. is indebted to MINECO for the “Ramon y Cajal” contract (ref: RyC-2015-18626), which is co-financed by the European Social Fund.

APPENDIX: DC Magnetic characterization

The magnetic characterization was performed through a commercial dc-squid magnetometer (MPMS2 by Quantum Device). Both the temperature dependent molar susceptibility χ_{mol}, in low field (H=10 Oe) and high field (H=10 kOe) conditions, and the isothermal magnetization for different temperatures were measured.

We discuss first the temperature behaviour $\chi_{mol}(T)$ at the low field for all the samples, then $\chi_{mol}(T)$ at the high field, and finally the isothermal magnetization measurements.

For the $Gd_2(Mo_{1-y}Mn_y)_2O_7$ samples the $\chi_{mol}(T)$ at 10 Oe (Fig. A.1) shows the expected ferromagnetic (FM)-like behavior typical for the undoped compound [44,58].

The inflection point of the susceptibility curve evidences the magnetic transition temperature as for the undoped compounds [14], which can be better visualized through a peak of $-d\chi/dT$ function occurring at T_p, indicated by an arrow in the inset of Fig. A.1. The magnetic transition is almost coincident with a bifurcation of the zero field cooling (ZFC) and field cooling (FC) curves at a temperature T_{ZFC-FC}, as previously observed for the undoped Gd parent compound at low magnetic field [44,58]. T_{ZFC-FC} and T_p are almost coincident for the low field measurements and their values, reported in Fig. 4, gradually diminish as a function of Mn content. This indicates a weakening of the FM correlations, induced by the Mn doping.

For the $Ho_2(Mo_{1-y}Mn_y)_2O_7$ samples the $\chi_{mol}(T)$ at 10 Oe (Fig. A.2) for all the Mn doping shows a small magneto-thermal hysteresis, evidenced by a bifurcation of ZFC and FC curves at T_{ZFC-FC}. This behavior is similar to the one of the undoped parent compound with A=Ho and many other lanthanides with small ionic radius [1,15,21,43]. In these compounds the small magneto-thermal hysteresis is a signature of a spin-glass behavior occurring below T_{ZFC-FC}, which for these compounds is defined as the freezing temperature T_f. It is worth noting that such temperatures are only slightly affected by the Mn doping (see Fig. 4).

For all the samples the high temperature behaviour $\chi_{mol}(T)$ at 10 Oe can be nicely fitted to a Curie-Weiss law. Fig. A.3 displays the $1/\chi_{mol}$ for all the $A_2(Mo_{1-y}Mn_y)_2O_7$ with A = Gd (left) and Ho (right) samples. The Curie constant, C, and the Curie-Weiss temperature, θ_{CW}, are determined by a linear fit of $1/\chi_{mol}(T)=(T-\theta_{CW})/C$ in the T-range 150-300 K. From the Curie constant we evaluated the free-ion effective magnetic moment μ_{eff}. The values of θ_{CW} and μ_{eff} are summarized in Table A.1 and displayed in Fig. A.4.

The Curie-Weiss temperature is positive for all the *A* = Gd samples, suggesting the presence of FM-like exchange interaction above the magnetic transition. Notably the Mn doping induces a strong reduction of θ_{CW}, indicating a weakening of the FM character consistent with the observed gradual reduction of the magnetic transition temperature. Differently from the Gd-based compounds, the Curie-Weiss temperature is always negative for all the $Ho_2(Mo_{1-y}Mn_y)_2O_7$ samples, suggesting the presence of AF-like exchange interactions between the magnetic ions above the T_f. The values of θ_{CW} stay almost constant indicating that the magnetic state is negligibly affected by the Mn doping.

Table A.1. Effective magentic moment (μ_{eff}) and Curie-Weiss temperaure (θ_{CW}) as obtained by linear fitting of $1/\chi_{mol}$ taken at 10 Gauss for 150<T<300 K for all the tested samples. The number in parentesys is the standar deviation of the last significative digit. The effective moments resulting from the Curie-Weiss fits should be compared to the expected values in the limit of non interagent paramagnetic moments: μ_{eff}^{TEO} (Gd)=7.94, μ_{eff}^{TEO} (Ho)=10.6. For the Gd-based undoped compound $\mu_{eff}^{undoped}$(Gd)=7.74(3) μ_B and $\theta_{CW}^{undoped}$(Gd)=57(2) K were determined at 10 kOe in Ref. [14].

$Gd_2(Mo_{1-y}Mn_y)_2O_7$	μ_{eff} (μ_B/ion)	θ_{CW} (K)
0.03	7.44(1)	+50.0(8)
0.05	7.79(1)	+29(6)
0.10	7.93(2)	+8(1)
$Ho_2(Mo_{1-y}Mn_y)_2O_7$		
0.03	10.315(9)	-8.0(4)
0.05	10.428(8)	-8.7(3)
0.10	11.012(8)	-10.2(4)

The free-ion effective magnetic moment μ_{eff} is in remarkable good agreement with the theoretical values of 7.94 μ_B and 10.6 μ_B expected for Gd^{3+} and Ho^{3+} free ions, respectively. Some small deviation might be likely due to the adopted fitting model which includes the contribution of all magnetic ions: the rare earth magnetic moment (dominant) and that of both Mo and Mn ions.

In order to further study the magnetic behaviour of the Mn doped compounds we also measured the magnetic susceptibility of all the samples at 10 kOe. A representative example of the ZFC-FC low temperature behaviour of χ_{mol}(T) at 10 kOe is shown in Fig. A.5 for the Gd and Ho samples with the highest Mn doping

content y = 0.10. The temperature transitions T_p and/or T_{ZFC-FC} are reported in Fig. 4 for all the samples. The increase of the magnetic field strongly affects the $\chi_{mol}(T)$ of the Ho series in a very similar way for all the Mn concentration, resembling the behavior of the undoped compounds [14] whose T_{ZFC-FC} is reduced from about 20 K (low field) down to less than 5 K (high field). The strong field dependence of the freezing temperature is the typical behavior of the $A_2(Mo_{1-y}Mn_y)_2O_7$ with spin-glass state character.

On the other hand, the increase of the magnetic field does not affect appreciably the magnetic transition $T_P \approx$ 60 K of the $Gd_2(Mo_{1-y}Mn_y)_2O_7$ for y = 0.03 (not shown), similarly to the case of the undoped Gd parent compound which presents mainly a broadening of the magnetic transition at 10 kOe [14] respect to the low field case [44,58]. We can safely assume that this is the typical behavior for the $A_2(Mo_{1-y}Mn_y)_2O_7$ compounds with FM character. In addition, no ZFC-FC splitting is observed at H=10 kOe down to 2 K for both for the parent undoped [14] and for y=0.03 (not shown). Interestingly, the Gd samples with y = 0.05 and 0.10 display a sizeable suppression of T_{ZFC-FC}, from 47 to 12 K and from 28 to 6 K, respectively. This clearly indicates that the Mn doping in $Gd_2(Mo_{1-y}Mn_y)_2O_7$ for y>0.03 not only weakens the FM character, as observed by the reduction of T_p, T_{ZFC-FC}, θ_{CW} measured at low field, but also drives the system towards a spin-glass phase.

The isothermal magnetizations of all the $A_2(Mo_{1-y}Mn_y)_2O_7$ doped samples are displayed in Fig. A.6 (for *A* = Gd) and Fig. A.7 (for *A* = Ho) as measured below and above the magnetic transition. All the samples display *i*) at high temperature a pure paramagnetic behavior, thus suggesting the absence of any ferromagnetic-like impurities with high T_C, and *ii*) at low temperature a "s-shape"-like behavior. For *A* = Gd a very small hysteresis cycle opens at low fields (Fig. A.6 panel b), which reflects the persistence of a FM character for all the Mn concentrations. For *A* = Ho the hysteresis cycles are fully closed (i.e. the coercitive field is zero) for all the Mn contents (not shown), as expected for a true spin-glass system. In this case the magnetization curves almost collapse on each other, providing a further proof that the spin-glass character is almost unperturbed by the Mn doping for *A* = Ho.

References

[1] J. S. Gardner, M. J. P. Gingras, J. E. Greedan, Magnetic pyrochlore oxides, Rev. Mod. Phys. 82 (2010) 53.

[2] Rodney C. Ewing, William J. Weber, Jie Lian, Nuclear waste disposal-pyrochlore $A_2B_2O_7$: Nuclear waste form for the immobilization of plutonium and ‘‘minor’’ actinides, J. Appl. Phys. 95 (2004) 5949.

[3] Yu-Jun Jin, Zhan-Guo Liu, Gui Cao, Wei Feng, Lei Chen, Yu-Jin Wang, Jia-Hu Ouyang, Order-disorder transition and electrical performance of $(Nd_{1-x}Y_x)_2Zr_2O_7$ solid solutions, J. Alloys Compd. 811 (2019) 151974.

[4] Kota Mitsumoto, Chisa Hotta, and Hajime Yoshino, Spin-Orbital Glass Transition in a Model of a Frustrated Pyrochlore Magnet without Quenched Disorder, Phys. Rev. Lett. 124 (2020) 087201.

[5] Zhen Song and Quanlin Liu, Tolerance factor, phase stability and order–disorder of the pyrochlore structure, Inorg. Chem. Front. 7 (2020) 1583.

[6] Chitrarasu Kaliyaperumal, Amirthapandian Sankarakumar, Thangadurai Paramasivam, Grain size engineering in nanocrystalline $Y_2Zr_2O_7$: A detailed study on the grain size correlated electrical properties, J. Alloys Compd. 831 (2020) 154782.

[7] Jianjun Wu, Fen Luo, Xiaoyan Shu, Shunzhang Chen, Guilin Wei, Bingsheng Li, Yi Xie, Wenqing Yuan, Facheng Yi, Xirui Lu, Immobilization of simulated waste into pure $Gd_2Zr_2O_7$ pyrochlore without space occupancy design, J Am. Ceram. Soc. 103 (2020) 4700.

[8] Zhe Tang, Zhangyi Huang, Wei Han, Jianqi Qi, Yanli Shi, Nannan Ma, Yutong Zhang, Xiaofeng Guo, and Tiecheng Lu, Uranium-Incorporated Pyrochlore $La_2(U_xMg_xZr_{1-2x})_2O_7$ Nuclear Waste Form: Structure and Phase Stability, Inorg. Chem. 59 (2020) 9919.

[9] G. Karthick, Anirudha Karati, B.S. Murty, Low temperature synthesis of nanocrystalline $Y_2Ti_2O_7$, $Y_2Zr_2O_7$, $Y_2Hf_2O_7$ with exceptional hardness by reverse co-precipitation technique, J. Alloys Compd. 837 (2020) 155491.

[10] T. Jiang, M. Xie, X. Wang, X. Song, Effects of Nb^{5+} doping on thermal properties of $Gd_2(Zr_{1-x}Nb_x)_2O_{7+x}$ ceramics, Adv. Appl. Ceram. 119 (2020) 212.

[11] Erkang Hu, Peijian Lin, Edwin Yue-Bun Pun, Jinliang Yuan, Hai Lin and Xin Zhao, Fluorescent Thermal Feedback in Ho^{3+}/Yb^{3+} Doped $Y_2Ti_2O_7$ Electrospun Nanofibers, J. Electrochem. Soc. 167 (2020) 027510.

[12] M.S. Koroleva, A.G. Krasnov, A. Senyshyn, A. Schökel, I.R. Shein, M.I. Vlasov, I.V. Piir, Structure, thermal stability, optoelectronic and electrophysical properties of Mg- and Na-codoped bismuth niobate pyrochlores: Experimental and theoretical study, J. Alloys Compd., https://doi.org/10.1016/j.jallcom.2020.157742.

[13] Prajyoti Singh, Arkadeb Pal, Vinod K. Gangwar, Prince K. Gupta, Mohd. Alam, Surajit Ghosh, R.K. Singh, A.K. Ghosh, Sandip Chatterjee, Wasp–Waisted loop and spin frustration in $Dy_{2-x}Eu_xTi_2O_7$ pyrochlore, J. Magn. Magn. Mater. 518 (2021) 167364.

[14] C. Castellano, G. Berti, F. Rubio Marcos, G. Lamura, S. Sanna, E. Salas-Colera, A. Brambilla, Á. Muñoz-Noval, L. Duò, F. Demartin, Anomalous local lattice disorder and distortion in $A_2Mo_2O_7$ pyrochlores, J. Alloys Compd. 723 (2017) 327.

[15] Y. Moritomo, Sh. Xu, A. Machida, T. Katsufuji, E. Nishibori, M. Takata, M. Sakata, S-W. Cheong, Chemical pressure control of exchange interaction in Mo pyrochlore, Phys. Rev. B 63 (2001) 144425.

[16] Y. Shimakawa and Y. Kubo, N. Hamada, J. D. Jorgensen, Z. Hu, and S. Short, M. Nohara and H. Takagi, Crystal structure, magnetic and transport properties, and electronic band structure of $A_2Mn_2O_7$ pyrochlores (A = Y , In, Lu, and Tl), Phys. Rev. B 59 (1999) 1249.

[17] J. B. Goodenough, An interpretation of the magnetic properties of the perovskite-type mixed crystals $La_{1-x}Sr_xCoO_{3-\lambda}$, J. Phys. Chem. Solids 6 (1958) 287.

[18] K. Taniguchi, T. Katsufuji, S. Iguchi, Y. Taguchi, H. Takagi, and Y. Tokura, Raman study of the metal-insulator transition in pyrochlore Mo oxides, Phys. Rev. B 70 (2004) 100401(R).

[19] N. Hanasaki, M. Kinuhara, I. Kézsmárki, S. Iguchi, S. Miyasaka, N. Takeshita, Mott-Anderson Transition Controlled by a Magnetic Field in Pyrochlore Molybdate, Phys. Rev. Lett. 96 (2006) 116403.

[20] J.A. Hodges, P. Bonville, A. Forget, J.P. Sanchez, P. Vulliet, M. Rams, and K. Królas, Magnetic properties of $Yb_2Mo_2O_7$ and $Gd_2Mo_2O_7$ from rare earth Mössbauer measurements, Eur. Phys. J. B 33 (2003) 173.

[21] H. Shinaoka, Y. Motome, T. Miyake, S. Ishibashi, Spin-orbital frustration in molybdenum pyrochlores $A_2Mo_2O_7$ (A = rare earth), Phys. Rev. B 88 (2013) 174422.
[22] T. Katsufuji, H.Y. Hwang, and S-W. Cheong, Anomalous Magnetotransport Properties of $R_2Mo_2O_7$ near the Magnetic Phase Boundary, Phys. Rev. Lett. 84 (2000) 1998.
[23] J.-G. Park, Younghun Jo, Junghwan Park, H.C. Kim, H.-C. Ri, Sh. Xu, Y. Moritomo, S.-W. Cheong, Electrical and magnetic properties of $R_2Mo_2O_7$ (R=Nd, Sm, Gd and Dy), Physica B 328 (2003) 90.
[24] N. Hanasaki, K. Watanabe, T. Ohtsuka, I. Kézsmárki, S. Iguchi, S. Miyasaka, and Y. Tokura, Nature of the Transition between a Ferromagnetic Metal and a Spin-Glass Insulator in Pyrochlore Molybdates, Phys. Rev. Lett. 99 (2007) 086401.
[25] G. Prando, P. Carretta, A. U. B. Wolter, R. Saint-Martin, A. Revcolevschi, and B. Büchner, Amorphous ferromagnetism and re-entrant magnetic glassiness in single-crystalline $Sm_2Mo_2O_7$, Phys. Rev. B 90 (2014) 085111.
[26] S. Iguchi, N. Hanasaki, M. Kinuhara, N. Takeshita, C. Terakura, Y. Taguchi, H. Takagi, and Y. Tokura, Emergence of a Diffusive Metal State with No Magnetic Order near the Mott Transition in Frustrated Pyrochlore-Type Molybdates, Phys. Rev. Lett. 102 (2009) 136407.
[27] Yukitoshi Motome and Nobuo Furukawa, Phase Competition in the Double-Exchange Model on the Frustrated Pyrochlore Lattice, Phys. Rev. Lett. 104 (2010) 106407.
[28] Single Crystal and Powder Diffraction − Freely Available Crystallographic Software for Academia: http://www.ccp14.ac.uk/mirror/mirror.htm
[29] O. Masson, Peakoc profile fitting program, 2008, http://www.esrf.eu/UsersAndScience/Experiments/TBS/SciSoft/OurSoftware/ PEAKOC
[30] G.R. Castro, Optical design of the general-purpose Spanish X-ray beamline for absorption and diffraction, J. Synchrotron Rad. 5 (1998) 657.
[31] B. H. Toby, EXPGUI, a graphical user interface for *GSAS*, J. Appl. Cryst. 34 (2001) 210.
[32] B. Ravel and M. Newville, ATHENA, ARTEMIS, HEPHAESTUS: data analysis for X-ray absorption spectroscopy using IFEFFIT, J. Synchrotron Radiat. 12 (2005) 537.
[33] J.J. Rehr, J.J. Kas, F.D. Vila, M.P. Prange, K. Jorissen, Parameter-free calculations of X-ray spectra with FEFF9, Phys. Chem. Chem. Phys. 12 (2010) 5503.
[34] C. Castellano, G. Berti, S. Sanna, R. Ruiz-Bustos, J. van Duijn, A. Brambilla, Á. Muñoz-Noval, P. Carretta, L. Duò, and F. Demartin, Evidence of local structural order and spin-lattice coupling in the frustrated pyrochlore $Y_2Ru_2O_7$, Phys. Rev. B 91 (2015) 224101.
[35] C. H. Booth, J. S. Gardner, G. H. Kwei, R. H. Heffner, F. Bridges, and M. A. Subramanian, Local lattice disorder in the geometrically frustrated spin-glass pyrochlore $Y_2Mo_2O_7$, Phys. Rev. B 62 (2000) R755.
[36] C. Castellano, M. Ferretti, A. Martinelli, and M. R. Cimberle, Structural and magnetic properties of Cu substituted manganites studied by EXAFS and dc magnetization measurements, J. Alloys Compd. 478 (2009) 479.
[37] Takeshi Hagiwara, Katsuhiro Nomura, Hiroyuki Kageyama, Differences in local structures around zirconium atoms in $Eu_2Zr_2O_7$ and $La_2Zr_2O_7$, Solid State Ionics 335 (2019) 32.
[38] V.V. Popov, A.P. Menushenkov, A. Yu Molokova , A.A. Ivanov, S.G. Rudakov, N.V. Boyko, A.A. Yastrebtsev, E.V. Khramov, R.D. Svetogorov, V.V. Kurilkin, V. Yu Murzin, A.B. Kalinko, K.V. Ponkratov, N.A. Tsarenko, I.V. Shchetinin, Rearrangement in the local, electronic and crystal structure of europium titanates under reduction and oxidation, J. Alloys Compd. 831 (2020) 154752.
[39] R. D. Shannon, Revised effective ionic radii and systematic studies of interatomic distances in halides and chalcogenides, Acta Cryst. A32 (1976) 751.
[40] M. Coduri, M. Scavini, M. Brunelli, P. Masala, In situ pair distribution function study on lanthanum doped ceria, Phys. Chem. Chem. Phys. 15 (2013) 8495.
[41] M. Coduri, M. Scavini, M. Brunelli, P. Masala, E. Pedrazzin, Structural characterization of Tb-and Pr-doped ceria, Solid State Ionics 268 (2014) 150.
[42] D. N. Argyriou, Measurement of the static disorder contribution to the temperature factor in cubic stabilized ZrO_2, J. Appl. Crystallogr. 27 (1994) 155.
[43] Naushad Ali, M.P Hill, Sunil Labroo, J.E Greedan, Magnetic and electrical properties of $R_2Mo_2O_7$ pyrochlore compounds, J. Sol. State Chem. 83 (1989) 178.
[44] I. Mirebeau, A. Apetrei, I. Goncharenko, D. Andreica, P. Bonville, J. P. Sanchez, A. Amato, E. Suard, W. A. Crichton, A. Forget, and D. Colson, Pressure-induced ferromagnet to spin-glass transition in $Gd_2Mo_2O_7$, Phys. Rev. B 74 (2006) 174414.

[45] N. Cao, T. Timusk, N. P. Raju, J. E. Greedan and P. Gougeon, Optical properties of pyrochlore oxides $R_2Mo_2O_{7-\text{ delta}}$ (R: Sm, Gd, and Ho), J. Phys.: Condens. Matter 7 (1995) 2489.
[46] E. D. Crozier, J. J. Rehr, and R. Ingalls, in: D. Koningsberger and R. Prins (Eds.), X-Ray Absorption: Principles, Applications, Techniques of EXAFS, SEXAFS, XANES, Wiley, New York, 1988, pp. 373-442.
[47] C. Castellano, G. Berti, M. Ferretti, A. Martinelli, M. R. Cimberle, Strong enhancement of the ferromagnetic phase and local order in Ru substituted manganites studied by EXAFS and dc magnetization measurements, J. Alloys Compd. 663 (2016) 560.
[48] G. Beni and P. M. Platzmann, Temperature and polarization dependence of extended x-ray absorption fine-structure spectra, Phys. Rev. B 14 (1976) 1514.
[49] N. W. Ashcroft and N. D. Mermin, in *Solid State Physics* (Saunders College, Philadelphia, 1976).
[50] M. B. Johnson, D. D. James, A. Bourque, H. A. Dabkowska, B. D. Gaulin, and M. A. White, Thermal properties of the pyrochlore, $Y_2Ti_2O_7$, J. Solid State Chem. 182 (2009) 725.
[51] G. Berti, S. Sanna, R. Ruiz-Bustos, J. van Duijn, A. Brambilla, Á. Muñoz-Noval, F. Demartin, L. Duò and C. Castellano, Evidence of a correlation between magnetic and structural transitions in $Y_{2-x}Zn_xRu_2O_7$ pyrochlore compounds, RSC Adv. 5 (2015) 100809.
[52] I. Mirebeau, A. Apetrei, I. Goncharenko, D. Andreica, P. Bonville, Magnetic transition induced by pressure in Gd2Mo2O7 as studied by neutron diffraction and μSR, J. Magn. Magn. Mater. 310 (2007) 919.
[53] A. Higashiya, S. Imada, A. Yamasaki, A. Irizawa, A. Sekiyama, S. Suga, Y. Taguchi, M. Iwama, K. Ohgushi, Y. Tokura, Electron correlation and the metal-insulator transition of the pyrochlore molybdates $R_2Mo_2O_7$ (R = Nd, Sm, Gd, Tb, Y), Phys. Rev. B 75 (2007) 155106.
[54] I. V. Solovyev, Effects of crystal structure and on-site Coulomb interactions on the electronic and magnetic structure of $A_2Mo_2O_7$ (A = Y , Gd, and Nd) pyrochlores, Phys. Rev. B 67 (2003) 174406.
[55] P. A. Lee, P. H. Citrin, P. Eisenberger, and B. M. Kincaid, Extended x-ray absorption fine structure—its strengths and limitations as a structural tool, Rev. Mod. Phys. 53 (1981) 769.
[56] T. Keiber, F. Bridges, and B. C. Sales, Lead Is Not Off Center in PbTe: The Importance of *r*-Space Phase Information in Extended X-Ray Absorption Fine Structure Spectroscopy, Phys. Rev. Lett. 111 (2013) 095504.
[57] P. E. R. Blanchard, R. Clements, B. J. Kennedy, C. D. Ling, E. Reynolds, M. Avdeev, A. P. J. Stampfl, Z. Zhang, and L.-Y. Jang, Does local disorder occur in the pyrochlore zirconates?, Inorg. Chem. 51 (2012) 13237.
[58] W. Schnelle and R. K. Kremer, Calorimetric study of the pyrochlore compounds $Gd_2Mo_2O_7$ and $Sm_2Mo_2O_7$, J. Phys.: Condens. Matter 16 (2004) S685.

Main Text Figure Captions

Fig. 1. (Color online) $k^2\chi$(k) EXAFS signals at selected measured temperatures between 5 K (lower curve) and 300 K (upper curve), for the $Ho_2(Mo_{0.95}Mn_{0.05})_2O_7$ compound. Data were offset for clarity.

Fig. 2. (Color online) Back Fourier transform best-fit curve and single fit contributions for the spectrum taken at 6.5 K on $Ho_2(Mo_{0.95}Mn_{0.05})_2O_7$. Letters refer to different paths as follows: (a) Data + fit; (b) Mo–O1.1–Mo (2 atoms); (c) Mo–Ho1.1–Mo; (d) Mo–Mo1.1–Mo; (e) Mo–O1.1–Mo–O1.1–Mo; (f) Mo–O1.1–Mo (4 atoms). Data have been offset for clarity.

Fig. 3. (Color online). Refined parameters versus T for $Gd_2Mo_2O_7$ (Gd0, black full circles), $Gd_2(Mo_{0.90}Mn_{0.10})_2O_7$ (Gd010, black empty circles), $Ho_2Mo_2O_7$ (Ho0, red full diamonds), $Ho_2(Mo_{0.90}Mn_{0.10})_2O_7$ (Ho010, red empty diamonds). (a) cell constants; (b) x_{O1} coordinate; (c) average atomic mean square parameter U_{ave}.

Fig. 4. (Color online) Mn-doping evolution of the magnetic transition temperature as measured by the peak derivative of the magnetic susceptibility (squares) and by the ZFC-FC bifurcation temperature (triangles) temperatures for H= 10 Oe (full symbol) and 10 kOe (open symbol) as obtained by DC magnetization measurements of $A_2(Mo_{1-y}Mn_y)_2O_7$ for A = Gd and Ho in the left and right panel, respectively. The data for y=0 are from Refs 14,44 and 45. The lines are only a guide for the eye.

Fig. 5. (Color online) Mo-O(1) first shell σ^2 ($Å^2$) as a function of temperature for a) $Gd_2Mo_2O_7$ and $Ho_2Mo_2O_7$ [3] and b) the corresponding Mn-doped (y = 0.05 and 0.10) compositions. The continuous line is the fit at high temperatures to a correlated Debye model plus a static offset. The axis scale is the same in both panels.

Fig. 6. (Color online) Bimodal distribution of the first shell Mo-O(1) interatomic distances for all the undoped and Mn-doped samples [N_{Mo-O} = 2 shorter apical (solid circles) and N_{Mo-O} = 4 longer basal (open circles) interatomic distances]. The statistical errors are equal to the dimensions of the circles.

Fig. 7. (Color online) Second shell Mo-*A* (solid circles) and Mo-Mo (open circles) interatomic distances. The statistical errors are equal to the dimensions of the circles.

Appendix Figure Captions

Fig. A.1. (Color online) Low-T dependence of the ZFC (open symbol) and FC (solid symbol) molar magnetic susceptibility for $Gd_2(Mo_{1-y}Mn_y)_2O_7$ samples with y=0.03 (square), 0.05 (circle) and y=0.10 (diamond) at H=10 Oe. The inset shows the temperature first derivative of the ZFC molar susceptibility - $d\chi_{mol}/dT$ for all the samples and the arrows indicate the peak temperature T_p, corresponding to the inflection point of χ_{mol} and almost coincident with the ZFC-FC bifurcation temperature T_{ZFC-FC}. For sake of clarity data for y=0.05 and 0.10 have been multiplied by a factor 2 and 10, respectively.

Fig. A.2. (Color online) Low-T dependence of the ZFC and FC molar magnetic susceptibility for $Ho_2(Mo_{1-y}Mn_y)_2O_7$ samples with y=0.03, 0.05 and y=0.10 at H=10 Oe.

Fig. A.3. (Color online) $1/\chi_{mol}(T)$ measured at 10 Oe for $A_2(Mo_{1-y}Mn_y)_2O_7$ with y=0.03, 0.05 and y=0.10 for *A* = Gd (left panel) and Ho (right panel) samples. The continuous lines are a linear fit in the T-range 150-300 K (see text for details).

Fig. A.4. (Color online) Effective magentic moment (μ_{eff}) (panel a) and Curie-Weiss temperature (θ_{CW}) (panel b) for the $A_2(Mo_{1-y}Mn_y)_2O_7$ as a function of Mn doping for *A* = Gd (cirlce) and Ho (square), as obtained by linear fitting of $1/\chi_{mol}(T)$ at 10 Oe for 150<T<300 K (see text).

Fig. A.5. (Color online) Representative low-T dependence of the ZFC and FC molar magnetic susceptibility of $A_2(Mo_{1-y}Mn_y)_2O_7$ samples for *A* = Gd (triangle) and Ho (circle) measured at high field H=10 kOe, with y=0.10. The arrows indicate the bifurcation temperature T_{ZFC-FC}.

Fig. A.6. (Color online) Field dependence of the mass magnetization of $Gd_2(Mo_{1-y}Mn_y)_2O_7$ with y=0.03, 0.05, 0.10 at T=5 K (lines) and 150 K (symbols). The bottom panel shows a zoom in the low field region for T=5 K which manifests a small hysteresis loop for all the Gd samples.

Fig. A.7. (Color online) Field dependence of the mass magnetization of $Ho_2(Mo_{1-y}Mn_y)_2O_7$ with y=0.03, 0.05, 0.10 at T=5 K (lines) and 50 K (symbols).

Main Text Figures

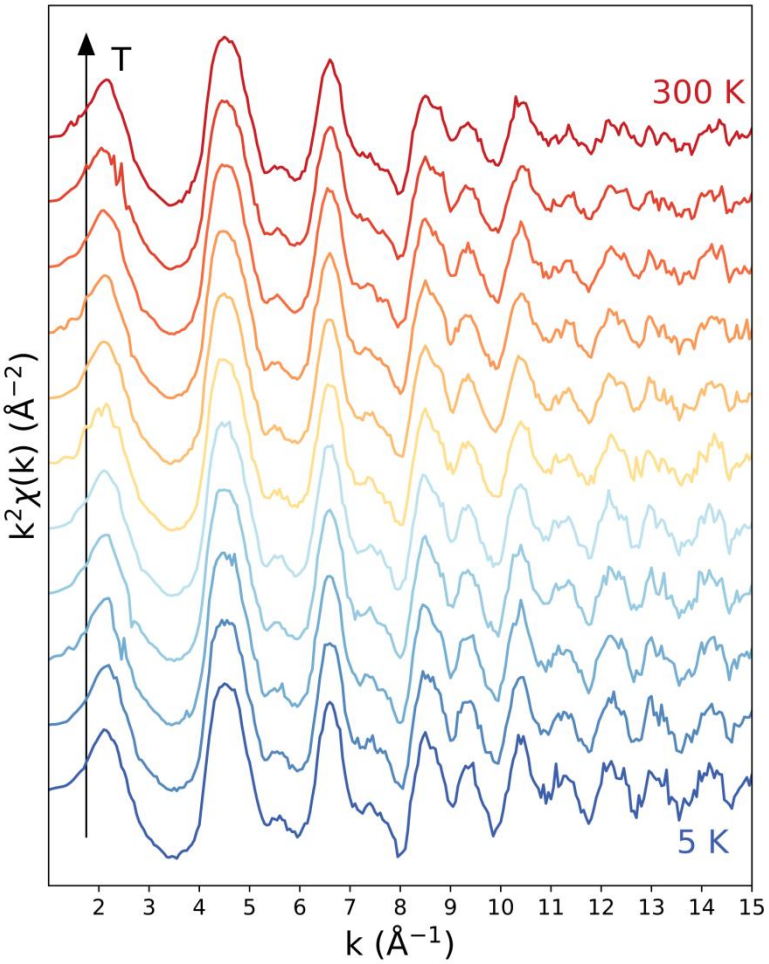

Fig. 1.

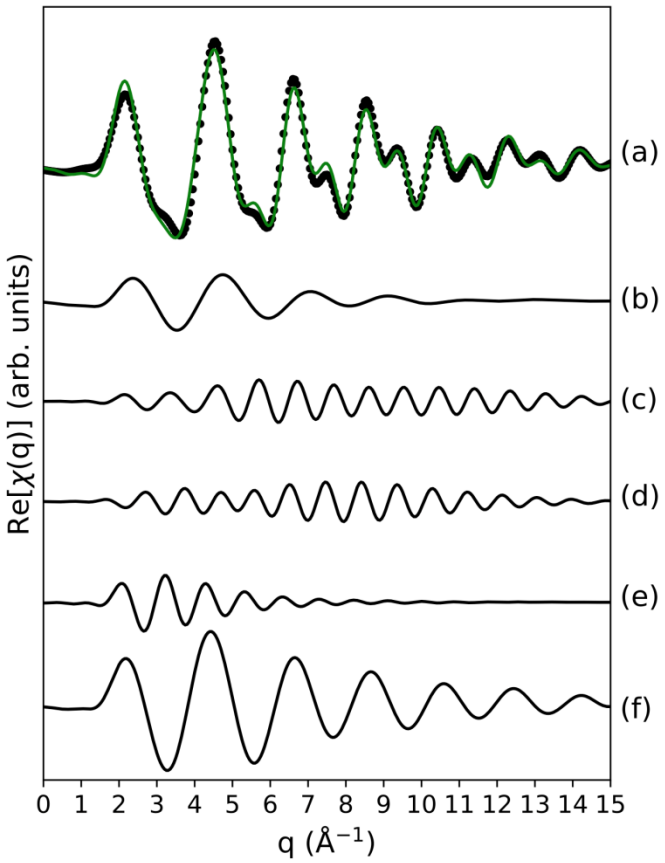

Fig. 2.

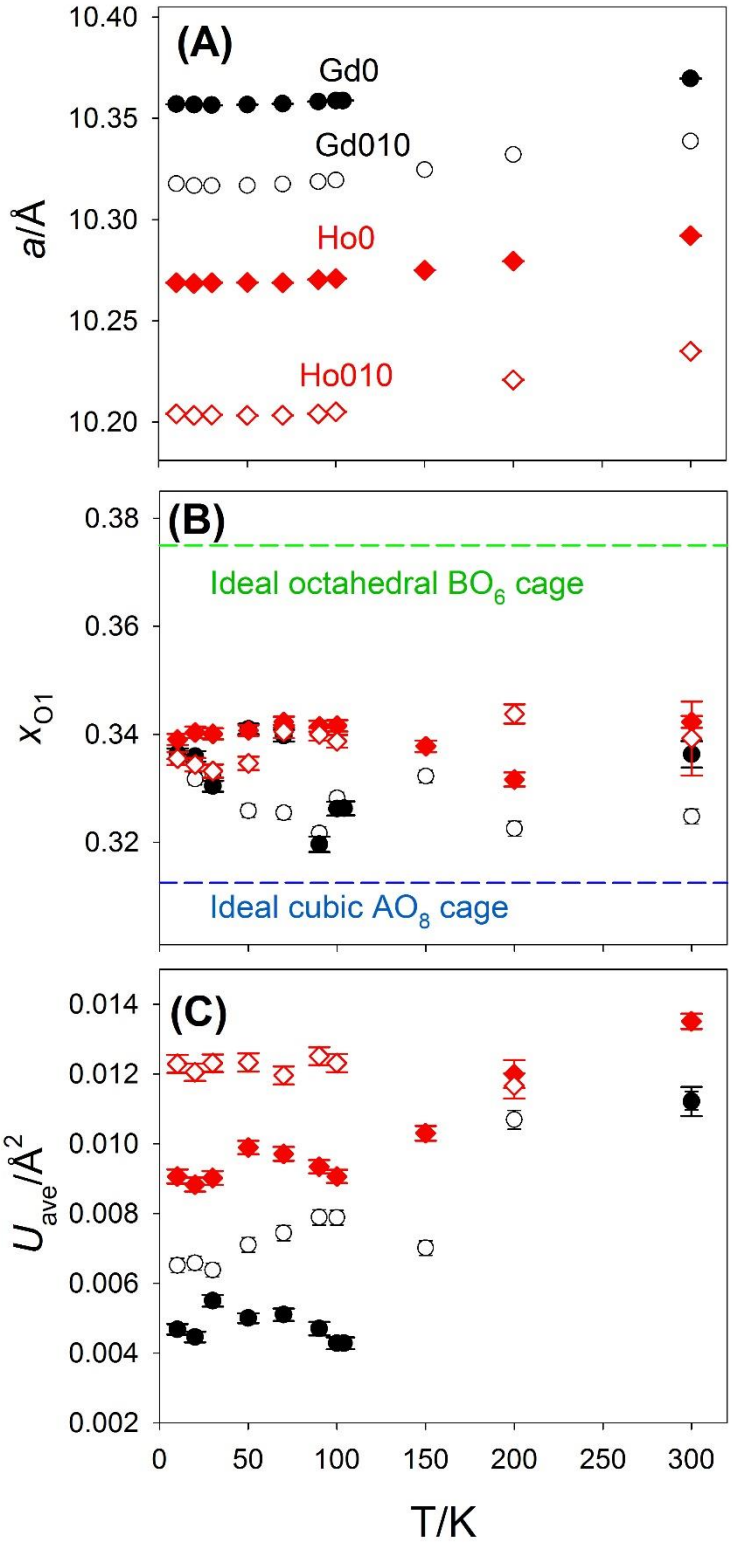
(A)
Gd0
Gd010
Ho0
Ho010
a/Å
10.40
10.35
10.30
10.25
10.20
(B)
Ideal octahedral BO6 cage
Ideal cubic AO8 cage
xO1
0.38
0.36
0.34
0.32
(C)
Uave/Å2
0.014
0.012
0.010
0.008
0.006
0.004
0.002
0
50
100
150
200
250
300
T/K

Fig. 3.

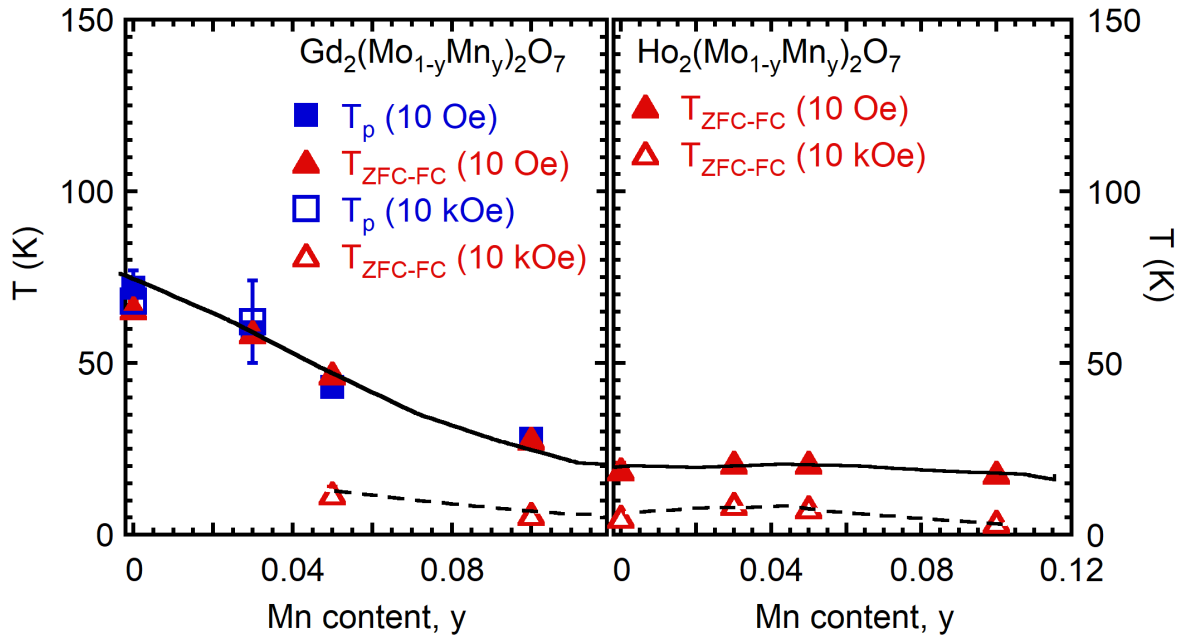
Gd2(Mo1-yMny)2O7
Tp (10 Oe)
TZFC-FC (10 Oe)
Tp (10 kOe)
TZFC-FC (10 kOe)
Ho2(Mo1-yMny)2O7
TZFC-FC (10 Oe)
TZFC-FC (10 kOe)
T (K)
Mn content, y
Mn content, y

Fig. 4.

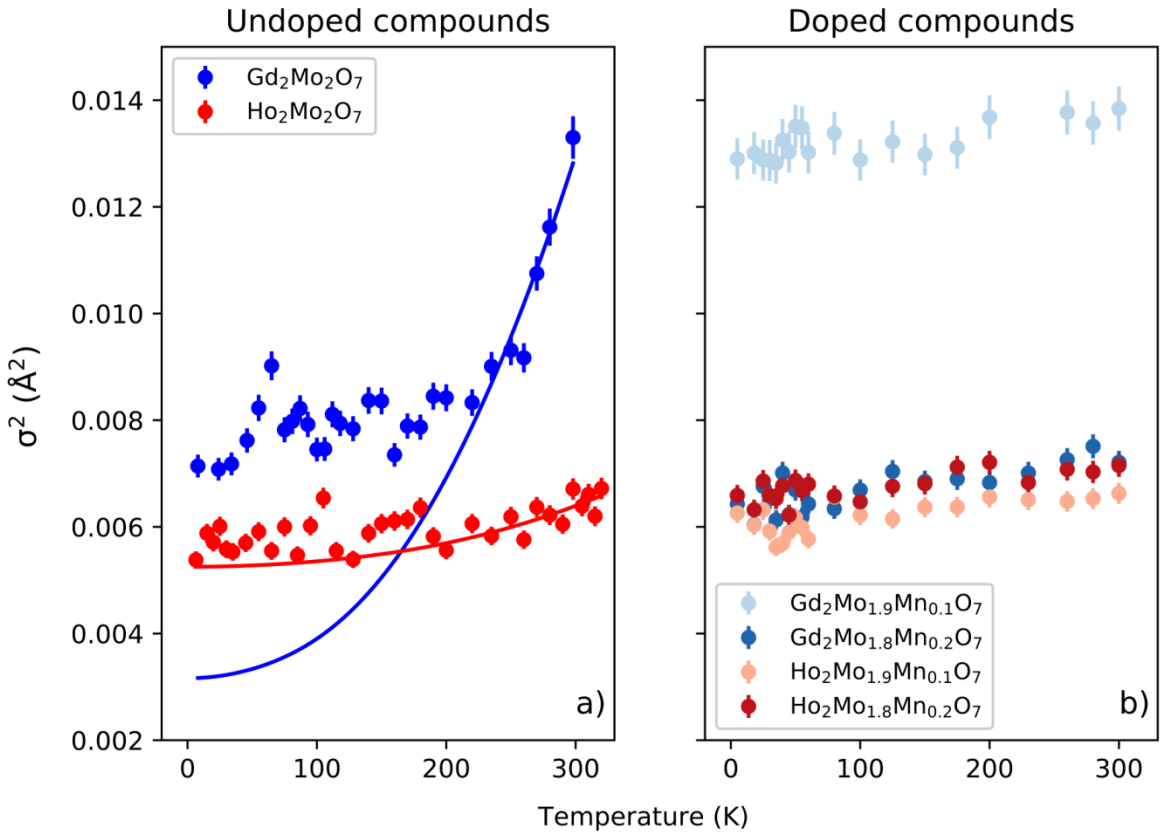
Undoped compounds
Doped compounds
Gd2Mo2O7
Ho2Mo2O7
Gd2Mo1.9Mn0.1O7
Gd2Mo1.8Mn0.2O7
Ho2Mo1.9Mn0.1O7
Ho2Mo1.8Mn0.2O7
σ2 (Å2)
Temperature (K)
a)
b)

Fig. 5.

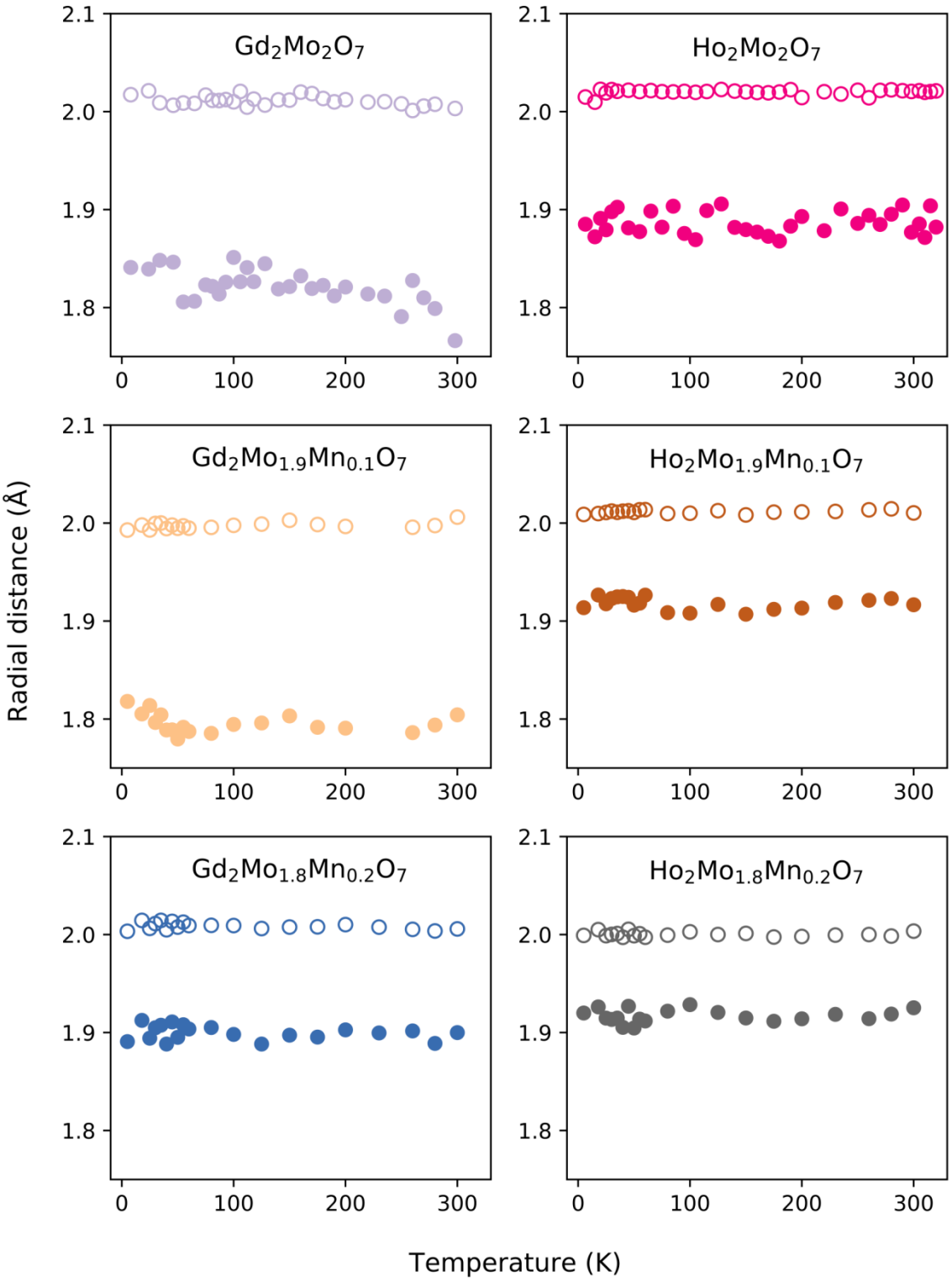
Gd2Mo2O7
Ho2Mo2O7
Gd2Mo1.9Mn0.1O7
Ho2Mo1.9Mn0.1O7
Gd2Mo1.8Mn0.2O7
Ho2Mo1.8Mn0.2O7
Radial distance (Å)
Temperature (K)
2.1
2.0
1.9
1.8
0
100
200
300

Fig. 6.

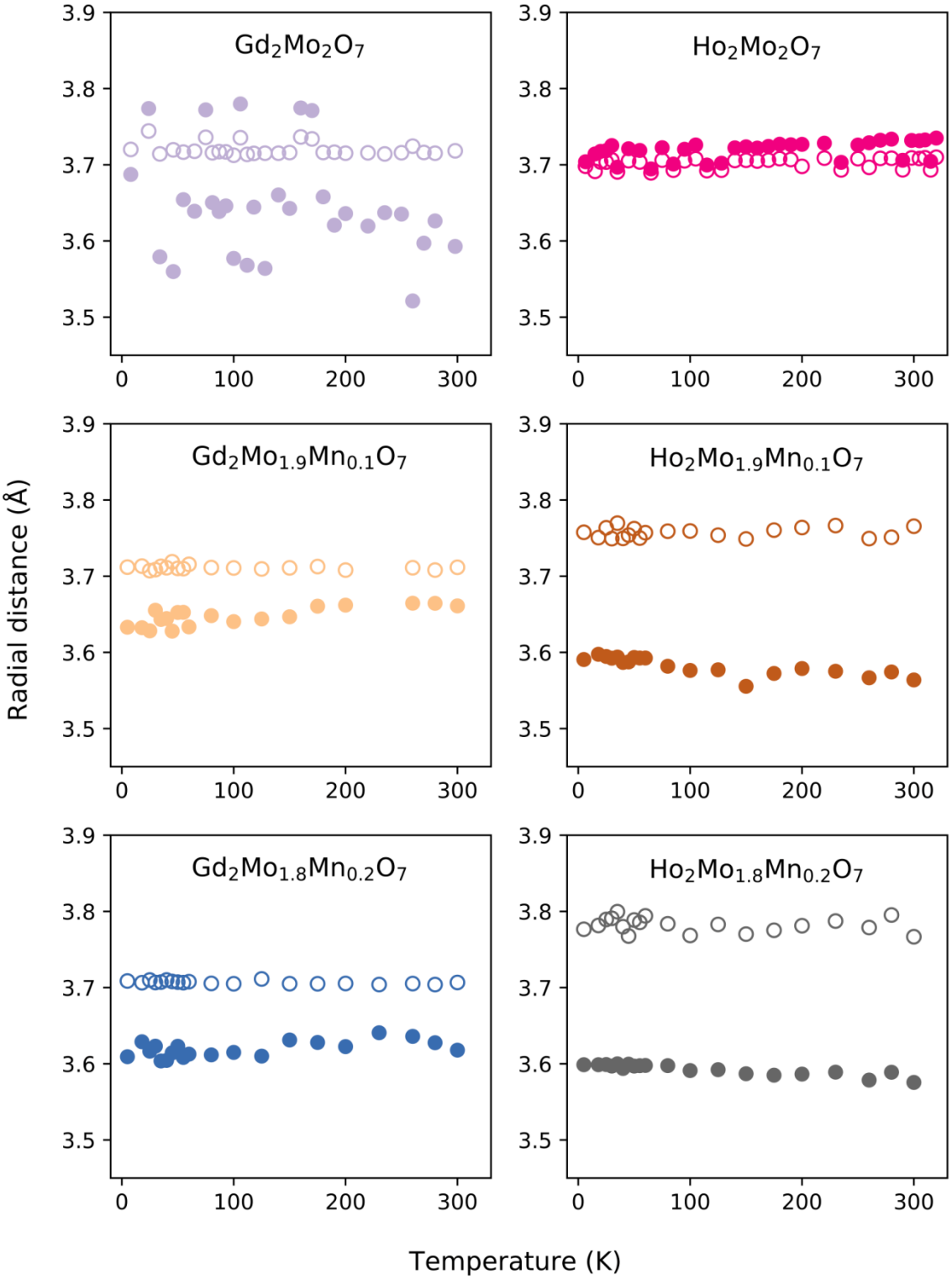
Gd2Mo2O7
Ho2Mo2O7
Gd2Mo1.9Mn0.1O7
Ho2Mo1.9Mn0.1O7
Gd2Mo1.8Mn0.2O7
Ho2Mo1.8Mn0.2O7
Radial distance (Å)
Temperature (K)
3.9
3.8
3.7
3.6
3.5
0
100
200
300

Fig. 7.

Appendix Figures

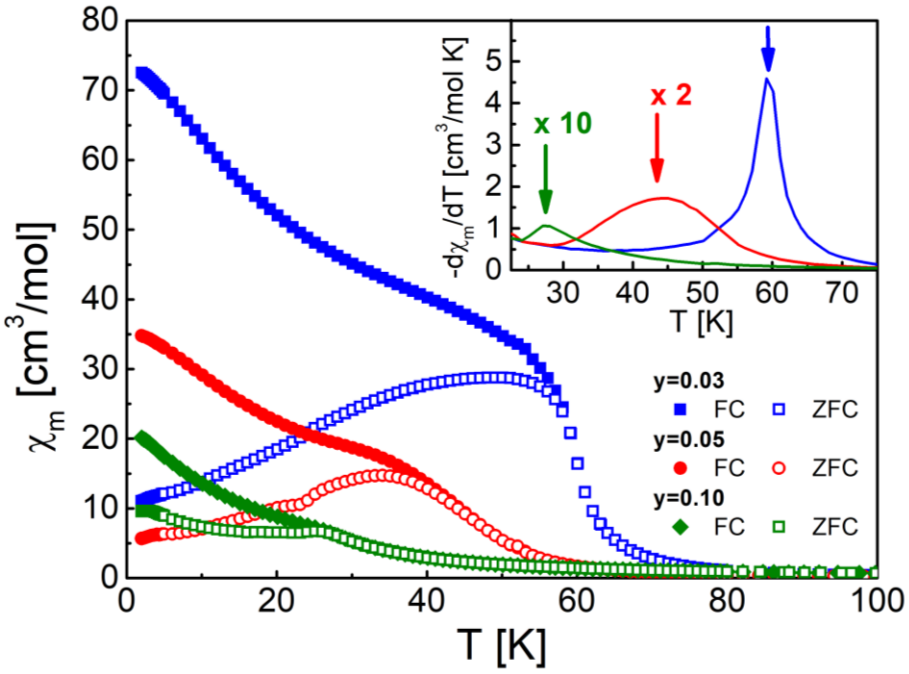

Fig. A.1.

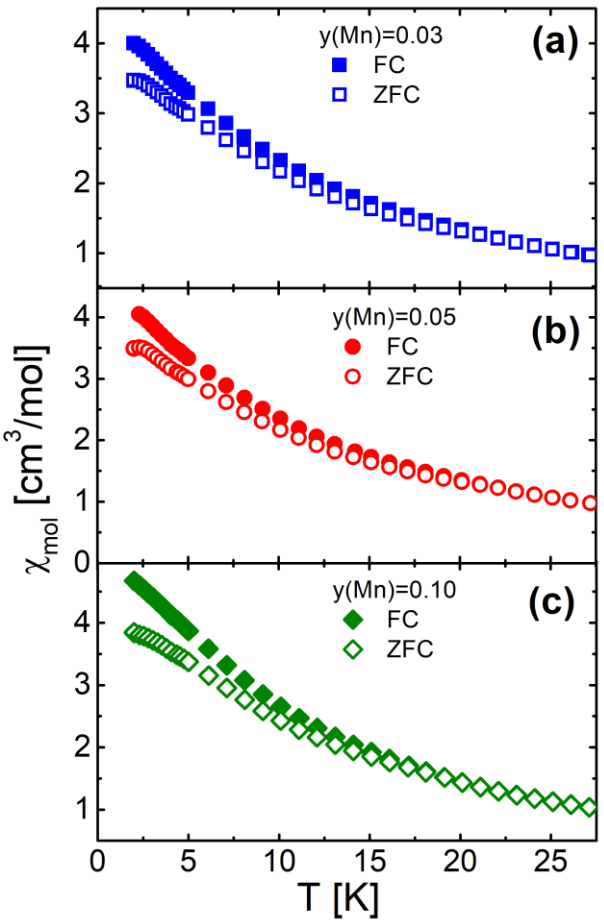
y(Mn)=0.03
FC
ZFC
(a)
y(Mn)=0.05
FC
ZFC
(b)
y(Mn)=0.10
FC
ZFC
(c)
χmol [cm3/mol]
T [K]
0
5
10
15
20
25
1
2
3
4

Fig. A.2.

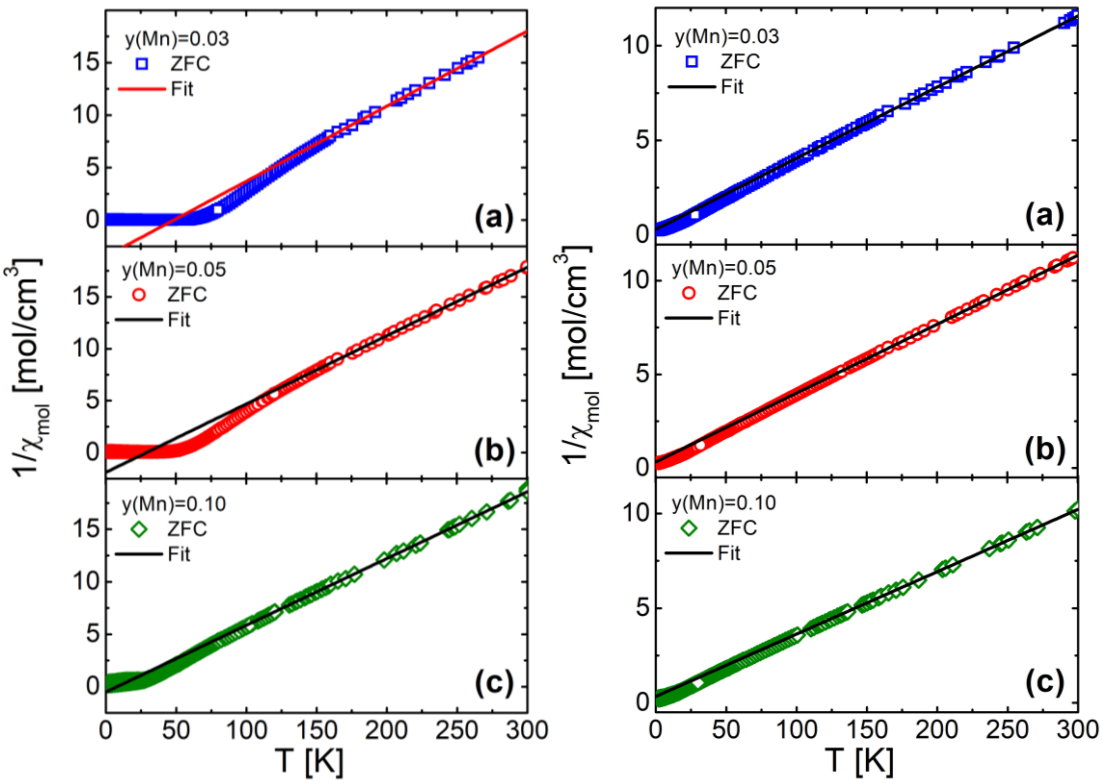
y(Mn)=0.03
ZFC
Fit
(a)
y(Mn)=0.05
ZFC
Fit
(b)
y(Mn)=0.10
ZFC
Fit
(c)
1/χmol [mol/cm3]
T [K]
0
50
100
150
200
250
300
0
5
10
15

.

Fig. A.3.

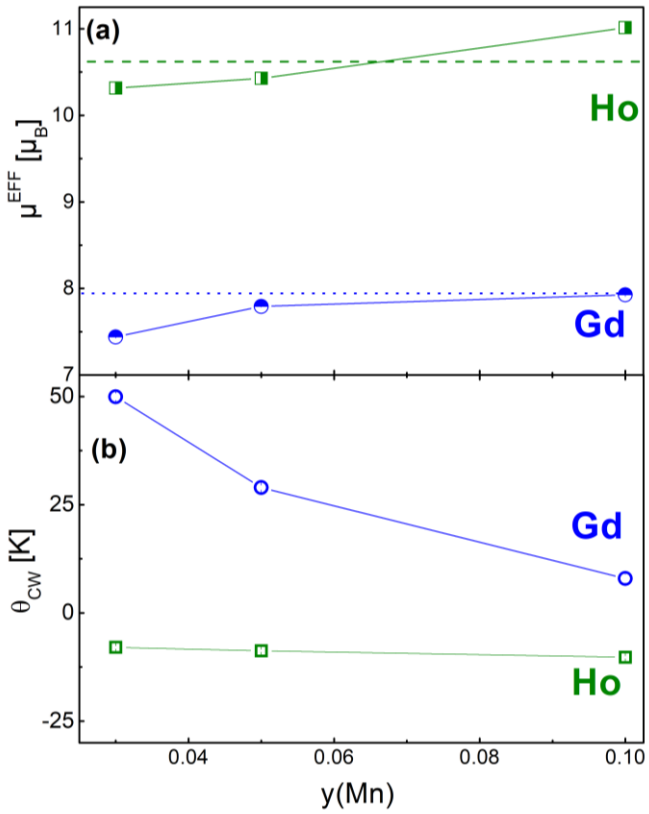
(a)
Ho
Gd
μ^{EFF} [μ_B]
11
10
9
8
7
(b)
Gd
Ho
θ_{CW} [K]
50
25
0
-25
0.04
0.06
0.08
0.10
y(Mn)

Fig. A.4.

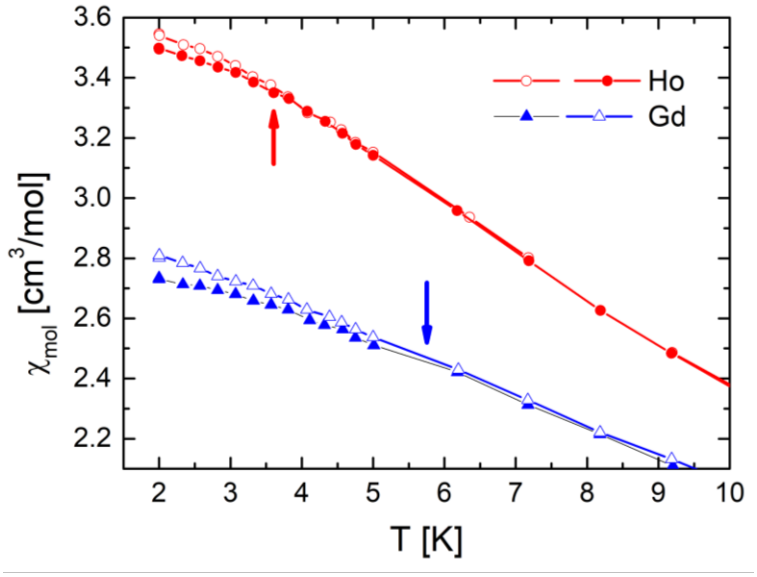
Ho
Gd
χ_{mol} [cm^3/mol]
T [K]

Fig. A.5.

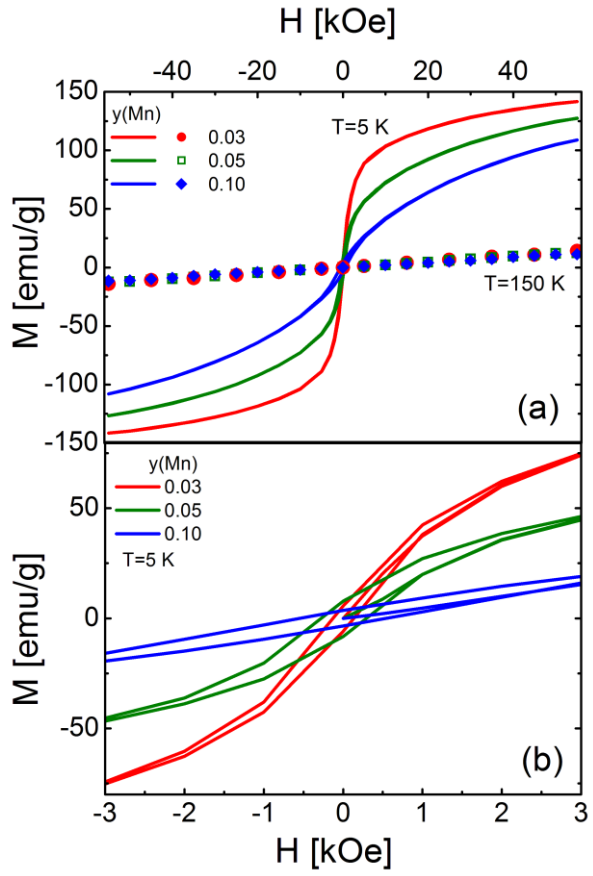
H [kOe]
y(Mn)
0.03
0.05
0.10
T=5 K
T=150 K
(a)
(b)
M [emu/g]
H [kOe]

Fig. A.6.

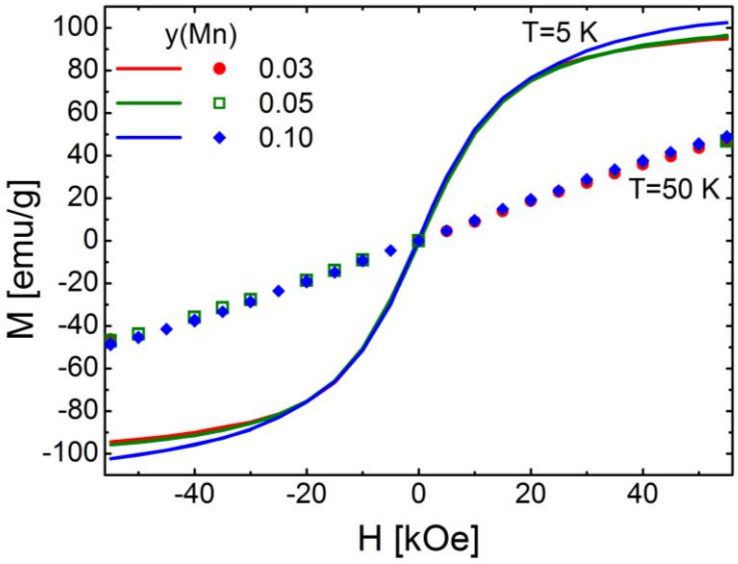
y(Mn)
0.03
0.05
0.10
T=5 K
T=50 K
M [emu/g]
H [kOe]
100
80
60
40
20
0
-20
-40
-60
-80
-100
-40
-20
0
20
40

Fig. A.7.